PCCP

ROYAL SOCIETY OF CHEMISTRY

PAPER

View Article Online
View Journal | View Issue

Cite this: *Phys. Chem. Chem. Phys.*, 2024, **26**, 27209

Asymmetric electron occupation of transition metals for the oxygen evolution reaction *via* a ligand–metal synergistic strategy†

Pai Wang,[a] Kunyu Li,[a] Tongwei Wu,[ab] Wei Ji[ac] and Yanning Zhang *[ab]

Received 12th August 2024,
Accepted 14th October 2024

DOI: 10.1039/d4cp03185g

rsc.li/pccp

The performance of two-dimensional transition-metal (oxy)hydroxides (TMOOHs) for the electrocatalytic oxygen evolution reaction (OER), as well as their large-scale practical applications, are severely limited by the sluggish kinetics of the four-electron OER process. Herein, using a symmetry-breaking strategy, we simulated a complex catalyst composed of a single Co atom and a 1,10-phenanthroline (phen) ligand on CoOOH through density functional theory studies, which exhibits excellent OER performance. The active site Co undergoes a valence oscillation between +2, +3 and even high valence +4 oxidation states during the catalytic process, resulting from the distorted coordination effect after the ligand modification. The induced asymmetry in the electronic states of surrounding nitrogen and oxygen atoms modulates the e_g occupation of Co-3d orbitals, which should be of benefit to reduce the overpotential in the OER process. By studying similar catalytic systems, the prominent role of ligands in creating asymmetric electronic structures and in modulating the valence of the active site and the OER performance was reconfirmed. This study provides a new dimension for optimizing the electrocatalytic performance of various TM–ligand complexes.

Introduction

With the easy preparation and adjustable electronic structure, transition-metal oxyhydroxides (TMOOHs) may exhibit excellent oxygen evolution reaction (OER) activity comparable to some commercial state-of-the-art Ir catalysts.[1–8] The valence state of the transition metal (TM) active center strongly contributes to the catalytic activity of OER electrocatalysts, and therefore constitutes an important parameter for the rational design of catalysts.[1,9,10] For example, the valence oscillation of Ni and Co in the cobalt-doped monolayer NiCo hydroxides can be attributed to the sequential dehydrogenation and deoxygenation processes.[11]

Tuning the spin and/or valence state through the structural symmetry-breaking has recently attracted great interest for the improvement of catalytic activity and selectivity. The symmetry-breaking strategy spontaneously rearranges the electron occupation of the active site and optimizes its orbital interaction with reactants, thereby optimizing the charge transfer between the two aspects.[12–17] For example, Zhang *et al.*[18] reported that the anodized Prussian blue analogue exhibited a volcanic relationship against the OER activity *via* increasing the valence state of Ni sites. Gao *et al.*[19] proved that the doping of electron-deficient boron in NiFeB hydroxide nanosheets promoted the oxidation of Ni^{2+} to a higher oxidation state Ni^{3+}, so as to enhance the OER activity. The valence change of metal sites is basically derived from the structural and electronic reconstruction in the electrochemical process.

How to connect the electron change of a TM with the catalytic activity calls for theoretical studies, so as to achieve a deep understanding of the nature of asymmetry regulation at the atomic level. Previous theoretical studies have made great contributions to the understanding of dynamic generation of the OER active sites on clean surfaces. However, real catalytic reactions usually take place on surfaces with various local disordering, in particular in any ligand–metal synergistic systems. It is thus instructive to investigate if the asymmetric manipulation of structural and electronic states changes the OER activity of the metal center on those complex surfaces.

Here, we broke the local structural symmetry of the Co@CoOOH monolayer through a ligand modification strategy, and performed density functional theory (DFT) studies on the intrinsic relationship between the electronic states of the active

[a] *Institute of Fundamental and Frontier Sciences, University of Electronic Science and Technology of China, Chengdu 611731, China. E-mail: yanningz@uestc.edu.cn*
[b] *Key Laboratory of Quantum Physics and Photonic Quantum Information, Ministry of Education, University of Electronic Science and Technology of China, Chengdu 611731, China*
[c] *Department of Physics, Renmin University of China, Beijing 100872, P. R. China*

† Electronic supplementary information (ESI) available. See DOI: https://doi.org/10.1039/d4cp03185g

Co site and its OER activity during the reaction process. It has been extensively shown in experiments that the bidentate ligand 1,10-phenanthroline (phen) effectively coordinates with metal centers, forming stable molecular structures on solid surfaces. Its strong coordination ability and rigid structure enhance the efficiency and tunability of catalytic reactions by restricting the geometric configuration of the metal coordination environment.[20,21] A new phen-Co@CoOOH catalyst synthesized by the adsorption of the phen ligand on the surface of CoOOH shows an excellent OER performance in alkaline solutions with a low overpotential of 0.38 V. Along with some systems of bpy(2,2′-bipyridine)-Co@CoOOH, bpy-Ni@NiOOH and phen-Ni@NiOOH, we demonstrated that the ligand–metal synergistic interaction causes asymmetry in both the local structure and the spin state of TM atoms. The distinguished valence oscillation of active sites upon the catalytic reaction could improve the OER performance. This work would prompt more attention to the valence oscillation behavior of symmetry-breaking electrocatalysts.

Computational details

Throughout the work, theoretical calculations were performed with the Vienna *ab initio* simulation package (VASP)[22,23] using the projector augmented wave (PAW)[24,25] method. The electronic exchange–correlation interactions were described within the generalized gradient approximation (GGA),[26,27] with the Perdew–Burke–Ernzerhof (PBE)[28,29] functional. The long-range van der Waals (vdW)[30,31] interactions of Grimme's DFT-D3 scheme were included. The Hubbard U term (DFT+U)[32] method was applied to accurately to correct the strong on-site Coulomb interactions of TM-3d states with a U_{eff} value of 3.0 eV for Co-d. An energy cutoff of 500 eV was used for the plane-wave expansion of the electronic eigenfunctions.

The bulk CoOOH was investigated using a (1 × 1) unit cell with a k-point grid of 9 × 9 × 2. The optimized lattice constants are $a = b = 2.86$ Å and $c = 12.98$ Å, which are in good agreement with the previously reported results.[33] We simulated ligand-anchoring CoOOH (001) surfaces by using four-atomic-layer slab models with a 5 × 5 supercell on the xy planar plane. A 15 Å vacuum is applied along the z direction to avoid the interactions between replicated images. The outermost atoms were fully relaxed till the convergence criteria of energy and force became less than 10^{-5} eV and 0.01 eV Å^{-1}, respectively. The Γ-centered 2 × 2 × 1 k-point grid was used to sample the Brillouin zone integration. For the OER calculations and electronic feature analyses of the phen-Ni@NiOOH system, the same U_{eff} value for Ni (2.0 eV) was adopted as that in our previous work on bpy-Ni@NiOOH.[34] For the transition state search, we used the climbing image-nudged elastic band (CI-NEB) method.[35]

Results and discussion

Electronic properties and OER activity

Both experimental and theoretical studies have proved that metal–ligand catalysts usually have excellent OER activity if their structural symmetry can be broken by the ligand modification.[36–42] In collaboration with excellent experiments,[34,43] we designed three different types of Co catalysts (Fig. 1a): pure CoOOH, Co@CoOOH

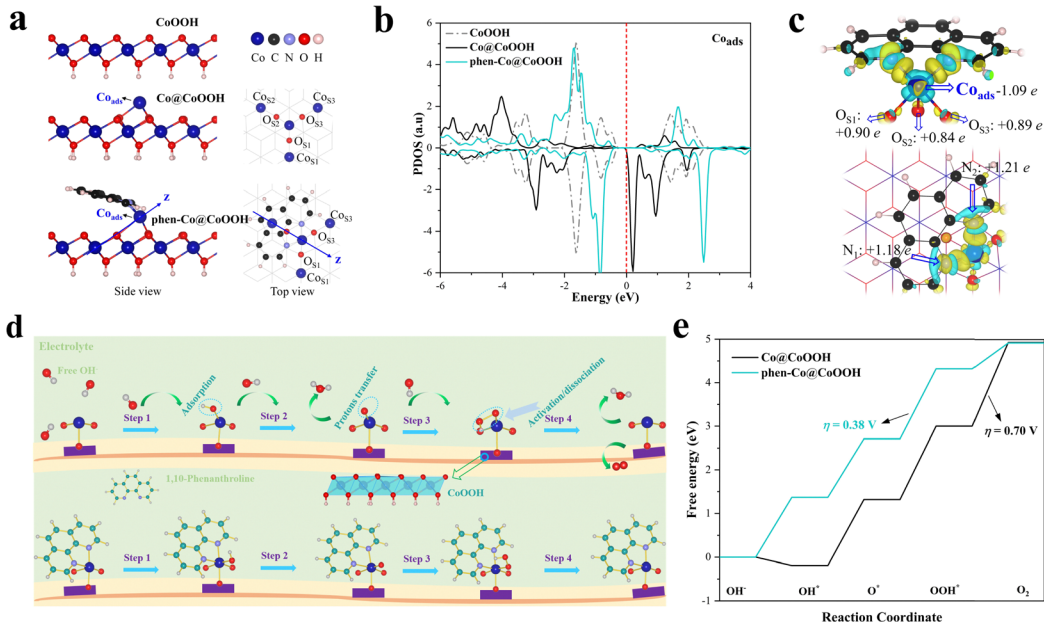

Fig. 1 DFT simulation of the alkaline OER reaction. (a) Structure diagrams of CoOOH, Co@CoOOH, and phen-Co@CoOOH systems; (b) corresponding PDOS of Co_{ads} (with energy scales in all PDOS figures aligned to the Fermi level, set as the zero point on the energy axis); (c) differential charge density on phen-Co@CoOOH. The cyan and yellow colors indicate electron depletion and accumulation, respectively, with an iso-surface value of 0.006 e bohr^{-3}; (d) illustration of reaction pathways of the OER on Co@CoOOH and phen-Co@CoOOH surfaces; and (e) the free energy profile of the oxygen evolution reaction for Co@CoOOH and phen-Co@CoOOH at 0 V *vs.* standard hydrogen electrode.

where a single Co atom (Co_{ads}) is stably adsorbed at the hollow site of the CoOOH surface to form a common tetrahedral crystal field with its nearest O_{S1-S3} atoms, and phen-Co@CoOOH where the phen ligand and the nearest-neighbor O atoms form a penta-coordinated square pyramidal geometry to the Co_{ads} atom (*cf.* Fig. S1, ESI† for the schematic diagram of the crystal field). The bond lengths between Co_{ads} and the two N atoms in phen are comparable to those of Co_{ads}–$O_{S1/S3}$ (see detailed values in Table S1, ESI†), which constitutes the *x*–*y* plane of the square pyramid. The Co_{ads}–O_{S2} bond length along the ligand direction is relatively longer (2.279 Å *vs.* 1.941 Å in Table S2, ESI†), forming the *z*-direction of the Jahn–Teller (JT) distortion.[44] Clearly, while the active sites of CoOOH are the edge Co atoms,[45] there are more anchored isolated Co atoms in Co@CoOOH and phen-Co@CoOOH, making the catalytic performance highly tunable.[46,47]

The projected electron density of states (PDOS) in Fig. 1b indicates that Co is a +3 cation in the low-spin (LS) state ($t_{2g}^6e_g^0$, $S = 0$) in the nonmagnetic CoOOH structure, which aligns with findings from other literature.[33,48] The PDOSs of Co@CoOOH and phen-Co@CoOOH surfaces are spin polarized, exhibiting total magnetic moments of 8.57 μ_B and 6.72 μ_B, respectively. With the introduction of the phen ligand, the occupied d-orbital PDOS of Co_{ads} in both the majority- and minority-spin channels become more localized near the Fermi level compared to the pure CoOOH system. The differential charge density of phen-Co@CoOOH in Fig. 1c depicts a significant charge transfer from Co_{ads} to the phen ligand, mainly concentrated in two N coordinations. The associated Bader charge analysis clearly suggests that the value of the nearest-neighbor O atom (O_{S2}) below the ligand is relatively smaller than those of the other two, implying that the local electronic structures around Co_{ads} become asymmetric due to the presence of the ligand.

The specific free energy (ΔG) for each elementary step was calculated to estimate the OER activity of Co@CoOOH and phen-Co@CoOOH structures, as displayed in Fig. 1d and e. For both systems, the adsorption of various intermediate species does not cause appreciable surface reconstruction and the OER process was performed through the adsorbate evolving mechanism (AEM). Energetically, all reaction steps involved in the OER process are up-hilled except the elementary step for the formation of OH* on Co@CoOOH (Fig. 1e). The rate-determining step (RDS) for the OER is the deprotonation and desorption of OOH* on the pristine Co@CoOOH with an overpotential of 0.70 V. The O* → OOH* conversion step becomes the RDS on phen-Co@CoOOH, leading to a reduced overpotential of about 0.38 V. Furthermore, we utilized the CI-NEB method to calculate the kinetic barriers of the RDS for both structures (Fig. S2, ESI†). While the RDS on Co@CoOOH exhibits a barrier of 0.47 eV, the RDS on phen-Co@CoOOH has a low barrier of 0.14 eV, suggesting that O–O bond formation is kinetically favorable. The phen ligand indeed accelerates OER catalysis both thermodynamically and kinetically.

Spin state and valence state changes of active sites

Detailed analyses of the local atomic arrangements and electronic states of the active center could be very helpful for a deep understanding of the structure–activity relationship.[49,50] It is well accepted that the spin density of Co_{ads} might be used a descriptor of the OER activity. As illustrated by the yellow isosurface contours in Fig. 2a, Co_{ads} in the pristine Co@CoOOH system keeps a large value of spin density during the reaction process. In contrast, in the phen-Co@CoOOH system (see Fig. 2b), Co_{ads} has fluctuating spin densities: the adsorption of OH* and OOH* on Co_{ads} decreases the spin density of Co_{ads} to almost zero, whereas there is a sharp increase upon O* adsorption. The occupancy of e_g orbitals in TM-based electrocatalysts strongly affects the electron spin state of Co_{ads}. The active metal atom with low or high e_g occupancy (corresponding to e_g^0 or e_g^2, respectively) would cause either a weak or strong binding with oxygen, both resulting in poor water splitting performance.[51,52] As confirmed later by the electronic arrangement analyses, the e_g occupancy of Co_{ads} (Fig. 2c) in the Co@CoOOH system is as high as 3, whereas the phen-Co@CoOOH system is in the low or intermediate state of 0–1.

To understand these changes, we may need to take into account the changes in Co_{ads} coordination that can be quantified by the bonding features of Co_{ads}–O_{S1-S3} shown in Fig. 2d and Table S1 (ESI†). The integrated crystal orbital Hamiltonian population (ICOHP) was combined to analyze the bonding of Co_{ads}–O_{S1-S3}. For the Co@CoOOH system, the average Co–O bonding changes only when Co_{ads} interacts with OH to be a complete tetrahedron in the first step. The subsequent intermediates exhibit a nearly unchanged coordination environment. The average bond length of Co_{ads}–O_{S1-S3} in phen-Co@CoOOH varies throughout the OER process, with a more significant change in the RDS (O* → OOH*). The oxidation states of Co_{ads} were obtained *via* the Bader analysis as plotted in Fig. 2e. The nonmagnetic Co_{S4} (Co^{3+}) atom on the substrate that is far away from Co_{ads} and the ligand (see Fig. S3, ESI† and the green/grey line in Fig. 2e) reveals an unchanged Bader charge (~ -1.27 *e*) during the OER process, and it is thus chosen as the reference state: whether Co_{ads} is transitioning from +3 to other valence states can be initially judged from the relative difference in the Bader charge observed between Co_{ads} and Co_{S4}. Differently from the relatively flat blue line in Fig. 2e, the Bader charge difference between Co_{ads} and Co_{S4} is relatively large for the phen-Co@CoOOH slab (-1.09 *e vs.* -1.27 *e*) and the O* (-1.37 *e vs.* -1.27 *e*) intermediate (indicated by the blue dashed circles), thus the valence state may oscillate.

We next analyzed the regulation of ligands on the electronic arrangement of Co_{ads}. As depicted in Fig. 3a, phen-Co@CoOOH exhibits three distinct oxidation states for Co_{ads} (Co^{2+}, Co^{3+} and Co^{4+}), corroborating the change in oxidation states as determined from Bader charge analysis. Here, to accurately distinguish the contributions from t_{2g} and e_g orbitals, as specified in Fig. S1 (ESI†) for phen-Co@CoOOH, we rotated the catalyst around TM_{ads} to match the axes of the TM_{ads}-d orbitals with the axes of the projection of the states within the VASP.[11,33,53] The PDOS diagram in Fig. 3b further shows that the initial Co_{ads} has three unoccupied states above the Fermi level (labelled in the Fig. 3b), corresponding to the +2 cation in the LS state ($t_{2g}^6e_g^1$, $S = 1$). Subsequently as shown in Fig. 3a, upon the OH*

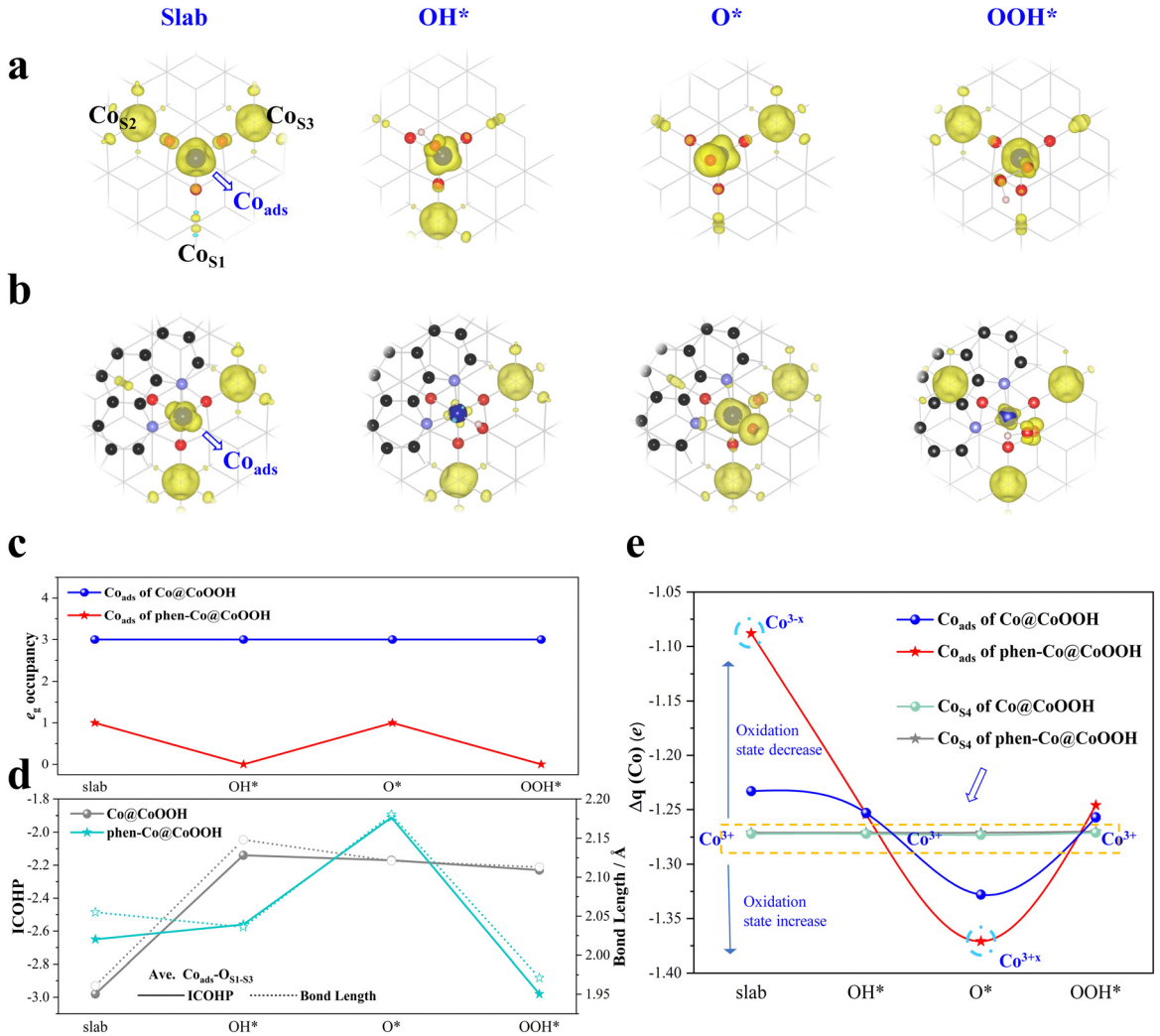

Fig. 2 Spin states and valence states of active sites. (a) Spin density of Co@CoOOH and its OER intermediates; (b) spin density of phen-Co@CoOOH and its intermediates. The iso-surface value is 0.014 e bohr^{-3}; (c) the occupancy of Co_{ads}-e_g electrons; (d) the evolution of ICOHP, bond length between involved average Co_{ads} and substrate O_{S1}; and (e) the corresponding Bader net charge diagram of Co_{S4} and Co_{ads}.

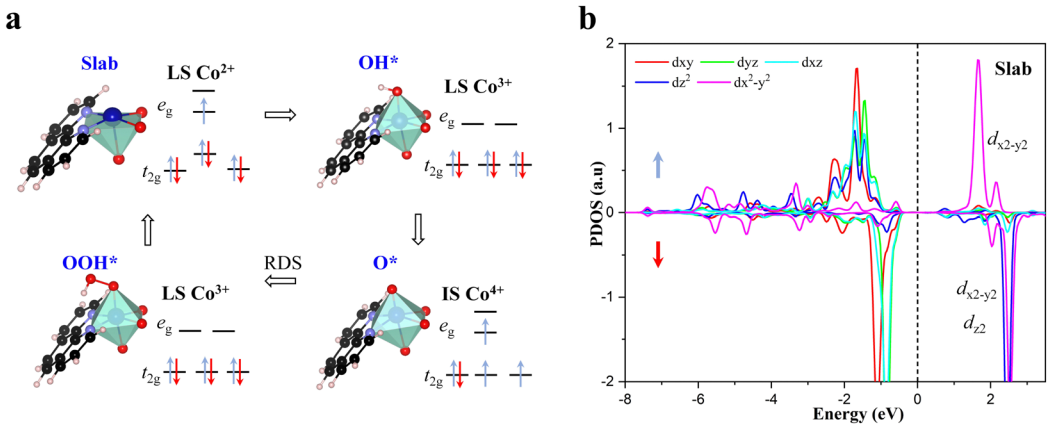

Fig. 3 Valence oscillation of the adsorption site, Co_{ads}. (a) Schematic diagrams of Co_{ads}-3d orbitals for phen-Co@CoOOH and its three OER intermediates; (b) the calculated partial density of states (PDOS) of Co_{ads}-3d orbitals for phen-Co@CoOOH. Spin electron occupations of d-orbitals are denoted as short arrows.

adsorption, there is the formation of a Co^{3+} LS state due to the presence of unoccupied e_g orbitals for Co_{ads} ($t_{2g}^6e_g^0$, $S = 0$) (see the corresponding PDOS in Fig. S4a, ESI†). The oxidation state of Co_{ads} becomes tetravalent (Co^{4+}) with an intermediate-spin (IS) state ($t_{2g}^4e_g^1$, $S = 1$) within the O* intermediate (*cf.* PDOS in Fig. S4b, ESI†). Finally, the coupling between adsorbed O* and OH^- preferentially fills the unpaired spin of IS Co^{4+} for a lower energy, leading to a smaller magnetization of the Co^{3+} LS state ($t_{2g}^6e_g^0$, $S = 0$) in the OOH* intermediate state (0.25 μ_B per Co_{ads} atom, PDOS in Fig. S4c, ESI†). Prior experiments have demonstrated that highly oxidized Ni^{4+} species are energetically favored by a $Ni^{2+} \rightarrow Ni^{3+} \rightarrow Ni^{4+}$ multistep evolution, and dynamically constructed Ni^{4+} species with high intrinsic activity drive the OER process.[54] Our results, through ligand modification, offer a theoretical explanation for the valence oscillation during the generation of highly oxidized +4 species in Co-based systems. The bond information of Co_{ads}-L (L = ligand atoms) in Table S2 (ESI†) indicates an obvious compression of the octahedron along the *z*-axis within the O* intermediate, causing the presence of the JT effect. With the formation of an O–O bond at the RDS, the Co_{ads}-L configuration returns to a cubic octahedron. The valence optimization thus arises from the alterations in the coordination environment around the active site, which changes the spin magnitude and serves as a crucial factor in enhancing OER performance.

As plotted in Fig. S5 (ESI†) for the electronic features of the Co@CoOOH system, the six valence electrons of Co_{ads} occupy d_{z^2} or $d_{x^2-y^2}$, d_{xy}, d_{xz}, and d_{yz} orbitals. The active site remains a high spin (HS) Co^{3+} ($t_{2g}^3e_g^3$, $S = 3$) state with no valence oscillation. We further replace the phen ligand with bpy in Co@CoOOH. The relevant valence state and its oscillation of Co_{ads} in the bpy-Co@CoOOH system is nearly identical to that in the phen-Co@CoOOH system, resulting in a minimal overpotential of 0.31 V shown in Fig. 4a and Fig. S6 (ESI†). Moreover, the oxygen evolution performance of the bpy-Ni@NiOOH catalyst studied in our previous work is nearly 58% higher than that of the uncoordinated bpy ligand (0.71 V *vs.* 0.30 V).[34] The intrinsic embodiment of this excellent catalytic effect is the synergistic effect between the ligand and metal atom, which regulates its local coordination environments and breaks the electronic symmetry of the active site. We provided detailed analyses of bpy-Co@CoOOH and see a clear charge transfer between the active site Co_{ads} and its surrounding N atoms in the ligand (Fig. 4b). This interaction makes the charge distributions of the nearest neighbor O_{S1-S3} atoms and the second nearest neighbor Co_{S1-S3} asymmetric, which further feeds back to the bonding effect between the active site and the TMOOH surface. As shown in Fig. 4c, the distance between the outermost atom of the ligand and the surface (marked as d_1) is 3.482 Å in bpy-Co@CoOOH, indirectly increasing d_2 to 1.308 Å (*vs.* 1.176 Å in Co@CoOOH). The average bond length of 2.267 Å in the *z* direction is longer than that of 1.926 Å in the *xy* direction. The spin density in Fig. 4d indicates that the magnetic moments of Co_{S2} and O_{S2} along the direction of the bpy ligand are nearly zero. Both the local coordination and electronic features of Co_{ads} verify the appearance of Jahn–Teller distortion, as illustrated in Fig. 4e. Only the d_{z^2} orbital of e_g states is occupied, an appreciable e_g occupation which is extremely beneficial to the adsorption of subsequent intermediates. We can find similar effects in the bpy-Ni@NiOOH system shown in Fig. S7(a)–(d) (ESI†).

This ligand–metal synergistic strategy may not be applicable to all complexes. For example, our calculations show that

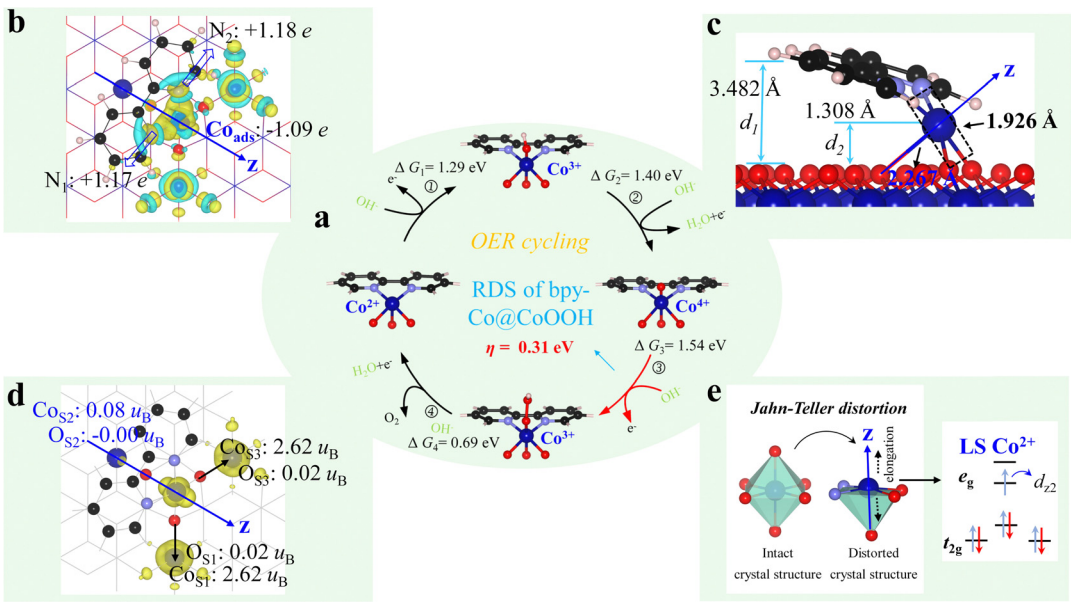

Fig. 4 Schematic diagram of the ligand modification strategy mechanism for bpy-Co@CoOOH. (a) Illustration of the OER pathway; (b) differential charge density. The cyan and yellow colors indicate electron depletion and accumulation, respectively, with an iso-surface value of 0.006 e $bohr^{-3}$; (c) sideview of bpy-Co@CoOOH to present the bond and distance information between the ligand and substrate; (d) spin density with an iso-surface value of 0.014 e $bohr^{-3}$; and (e) Jahn–Teller distortion and the corresponding electronic arrangement.

Ni@NiOOH with the coordination effect of the phen ligand has the lowest catalytic activity among the systems discussed here, with an overpotential of 1.71 V. The Bader charge analysis results in Fig. S7e (ESI†) show comparable values between Ni_{ads} and N, and thus the ligand should have less modification to the active site. The average bond difference between *z* and *xy* directions, as well as the magnetic moments of O_{S1-S3}/Co_{S1-S3} atoms displayed in Fig. S7(f)–(h) (ESI†), demonstrate that the ligands did not break the structural and electronic symmetries around Ni_{ads}. There is no JT distortion and the e_g occupancy number is 2. Along with the electronic arrangement of the active sites in these systems (Fig. S8, ESI†), it reveal again the key role of a moderate number of e_g occupancy in the improvement of OER performance. For such systems, efforts are currently being made through double-site synergy or doping with heterogeneous elements. These ongoing studies have indicated somewhat improved catalytic performance achieved using the phen-Ni@NiOOH system.

Although the above calculations using the charge-neutral method (CNM) have predicted nice catalyst candidates, it is necessary to consider their performance under realistic electrochemical conditions, in particular the effects of potential.[55–57] Combining the charge-extrapolation method proposed by Nørskov and co-workers,[58] we calculated the potential-dependent barriers and corrected the CI-NEB results for the Co@CoOOH and phen-Co@CoOOH catalysts. We observed an excellent linear correlation (Fig. S9, ESI†) between the amount of electron transfer and relative work function (Φ), at the initial, transition and final states. The extrapolated activation energy barriers (E_a) of the RDS (OOH* → O_2) are 0.47 eV for Co@CoOOH and 0.14 eV for phen-Co@CoOOH (O* → OOH*). These results indicate that with potential effects, the formation of OOH* species of phen-Co@CoOOH is still kinetically favorable. Please note that the E_a values for the RDS step remain the same before and after the extrapolation because the difference between Φ_{TS} and Φ_{IS} is close to zero.[58,59]

We also included four explicit water molecules above the active site of phen-Co@CoOOH with O* and OOH* adsorption, so as to stimulate a solvation shell environment (Fig. S10, ESI†). Free energy calculations show an RDS energy of 1.44 eV (*vs.* the original 1.61 eV), demonstrating that our catalyst also exhibits an excellent performance in a solvent environment.

Conclusions

In this paper, a coordination complex composed of an additional Co atom and a phen ligand was assembled into a layered Co@CoOOH surface, which exhibited a superb catalytic activity toward the OER due to the ligand modification strategy. The results of DFT calculations revealed that the active Co in phen-Co@CoOOH undergoes a valence oscillation between +2, +3 and high valence +4 during the oxygen evolution process. The spin state of phen-Co@CoOOH catalysts is modulated from the intermediate spin state to the low spin state, which benefits the formation of an O–O bond to further decrease the Gibbs free energy of the RDS (O* → OOH*). The ligand and TM site substitution strategies also work in two similar systems of bpy-Co@CoOOH and bpy-Ni@NiOOH. The structural and electronic symmetries of the nearest-neighbor atoms around the active site were broken, leading to an appropriate e_g occupation of TM atoms. The charge transfer between the ligand and the TM active sites plays a nonnegligible role in creating these asymmetries. Our work provides a route for rationally modulating the local structure, spin states, and valence of TM-based electrocatalysts by assembling ligands into TMOOH while improving the thermodynamics and kinetics of the OER. This can be applied to the design and development of multifunctional catalysts for various electrochemical reactions important for renewable energy conversion.

Data availability

The data supporting this article have been included as part of the ESI.†

Conflicts of interest

There are no conflicts to declare.

Acknowledgements

Yanning Zhang acknowledges the funding support from the Natural Science Foundation of Sichuan Province (No. 2023NSFSC0320). Tongwei Wu gratefully acknowledges support by the National Natural Science Foundation of China (No. 52202214) and Natural Science Foundation of Sichuan Province (No. 2023NSFSC0954). The numerical calculations in this study have been done on Hefei advanced computing center.

References

1 C. Qiao, Y. Hao, C. Cao and J. Zhang, *Nanoscale*, 2023, **15**, 450–460.
2 R.-Y. Fan, H.-Y. Zhao, Z.-Y. Zhao, W.-H. Hu, X. Liu, J.-F. Yu, H. Hu, Y.-M. Chai and B. Dong, *Nano Res.*, 2022, **16**, 12026–12034.
3 W. H. Lee, M. H. Han, Y.-J. Ko, B. K. Min, K. H. Chae and H.-S. Oh, *Nat. Commun.*, 2022, **13**, 605.
4 C. Feng, Z. Zhang, D. Wang, Y. Kong, J. Wei, R. Wang, P. Ma, H. Li, Z. Geng, M. Zuo, J. Bao, S. Zhou and J. Zeng, *J. Am. Chem. Soc.*, 2022, **144**, 9271–9279.
5 S. Li, R. Ma, J. Hu, Z. Li, L. Liu, X. Wang, Y. Lu, G. E. Sterbinsky, S. Liu, L. Zheng, J. Liu, D. Liu and J. Wang, *Nat. Commun.*, 2022, **13**, 2916.
6 H. Xiao, H. Shin and W. A. Goddard, *Proc. Natl. Acad. Sci. U. S. A.*, 2018, **115**, 5872–5877.
7 Y. Ding, J. Du, T. Wang and L. Sun, *CCS Chem.*, 2024, **6**, 365–376.
8 Y. Zhao, Q. Wen, D. Huang, C. Jiao, Y. Liu, Y. Liu, J. Fang, M. Sun and L. Yu, *Adv. Energy Mater.*, 2023, **13**, 2370038.

9 L. Li, X. Cao, J. Huo, J. Qu, W. Chen, C. Liu, Y. Zhao, H. Liu and G. Wang, *J. Energy Chem.*, 2023, **76**, 195–213.
10 H. Sun, X. Xu, Y. Song, W. Zhou and Z. Shao, *Adv. Funct. Mater.*, 2021, **31**, 2009779.
11 J. Kang, X. Qiu, Q. Hu, J. Zhong, X. Gao, R. Huang, C. Wan, L.-M. Liu, X. Duan and L. Guo, *Nat. Catal.*, 2021, **4**, 1050–1058.
12 G. Zhou, P. Wang, B. Hu, X. Shen, C. Liu, W. Tao, P. Huang and L. Liu, *Nat. Commun.*, 2022, **13**, 4106.
13 X. Mu, X. Gu, S. Dai, J. Chen, Y. Cui, Q. Chen, M. Yu, C. Chen, S. Liu and S. Mu, *Energy Environ. Sci.*, 2022, **15**, 4048–4057.
14 X. Wang, X. Zhou, C. Li, H. Yao, C. Zhang, J. Zhou, R. Xu, L. Chu, H. Wang, M. Gu, H. Jiang and M. Huang, *Adv. Mater.*, 2022, **34**, 2204021.
15 Z.-D. He, R. Tesch, M. J. Eslamibidgoli, M. H. Eikerling and P. M. Kowalski, *Nat. Commun.*, 2023, **14**, 3498.
16 Z. Zhang, P. Ma, L. Luo, X. Ding, S. Zhou and J. Zeng, *Angew. Chem., Int. Ed.*, 2023, **62**, e202216837.
17 H. Wang, T. Zhai, Y. Wu, T. Zhou, B. Zhou, C. Shang and Z. Guo, *Adv. Sci.*, 2023, **10**, 2301706.
18 H. Zhang, P. Li, S. Chen, F. Xie and D. J. Riley, *Adv. Funct. Mater.*, 2021, **31**, 2106835.
19 Y. Bai, Y. Wu, X. Zhou, Y. Ye, K. Nie, J. Wang, M. Xie, Z. Zhang, Z. Liu, T. Cheng and C. Gao, *Nat. Commun.*, 2022, **13**, 6094.
20 C. Queffélec, P. B. Pati and Y. Pellegrin, *Chem. Rev.*, 2024, **124**, 6700–6902.
21 L. Bai, C.-S. Hsu, D. T. L. Alexander, H. M. Chen and X. Hu, *J. Am. Chem. Soc.*, 2019, **141**, 14190–14199.
22 G. Kresse and J. Furthmüller, *Comput. Mater. Sci.*, 1996, **6**, 15–50.
23 G. Kresse and J. Furthmüller, *Phys. Rev. B: Condens. Matter Mater. Phys.*, 1996, **54**, 11169–11186.
24 P. E. Blöchl, *Phys. Rev. B: Condens. Matter Mater. Phys.*, 1994, **50**, 17953–17979.
25 G. Kresse and D. Joubert, *Phys. Rev. B: Condens. Matter Mater. Phys.*, 1999, **59**, 1758–1775.
26 J. P. Perdew, J. A. Chevary, S. H. Vosko, K. A. Jackson, M. R. Pederson, D. J. Singh and C. Fiolhais, *Phys. Rev. B: Condens. Matter Mater. Phys.*, 1992, **46**, 6671–6687.
27 J. P. Perdew, K. Burke and Y. Wang, *Phys. Rev. B: Condens. Matter Mater. Phys.*, 1996, **54**, 16533–16539.
28 J. P. Perdew, K. Burke and M. Ernzerhof, *Phys. Rev. Lett.*, 1996, **77**, 3865–3868.
29 J. P. Perdew, K. Burke and M. Ernzerhof, *Phys. Rev. Lett.*, 1997, **78**, 1396.
30 S. Grimme, J. Antony, S. Ehrlich and H. Krieg, *J. Chem. Phys.*, 2010, **132**, 154104.
31 S. Grimme, S. Ehrlich and L. Goerigk, *J. Comput. Chem.*, 2011, **32**, 1456–1465.
32 S. L. Dudarev, G. A. Botton, S. Y. Savrasov, C. J. Humphreys and A. P. Sutton, *Phys. Rev. B: Condens. Matter Mater. Phys.*, 1998, **57**, 1505–1509.
33 F. Li, H. Ai, D. Liu, K. H. Lo and H. Pan, *J. Mater. Chem. A*, 2021, **9**, 17749–17759.
34 P. Zhang, P. Wang, W. Wang, Q. Wu, M. Xiao, R. Alberto, Y. Zhang and C. Cui, *ACS Appl. Mater. Interfaces*, 2021, **13**, 48661–48668.
35 G. Henkelman, B. P. Uberuaga and H. Jónsson, *J. Chem. Phys.*, 2000, **113**, 9901–9904.
36 B. Das, A. Rahaman, A. Shatskiy, O. Verho, M. D. Kärkäs and B. Åkermark, *Acc. Chem. Res.*, 2021, **54**, 3326–3337.
37 C.-F. Li, J.-W. Zhao, L.-J. Xie, J.-Q. Wu, Q. Ren, Y. Wang and G.-R. Li, *Angew. Chem., Int. Ed.*, 2021, **60**, 18129–18137.
38 Z. Li, X. Zhang, Y. Kang, C. C. Yu, Y. Wen, M. Hu, D. Meng, W. Song and Y. Yang, *Adv. Sci.*, 2021, **8**, 2002631.
39 Y. Peng, Q. Liu, B. Lu, T. He, F. Nichols, X. Hu, T. Huang, G. Huang, L. Guzman, Y. Ping and S. Chen, *ACS Catal.*, 2021, **11**, 1179–1188.
40 A. E. Thorarinsdottir and D. G. Nocera, *Chem. Catal.*, 2021, **1**, 32–43.
41 W. Huang, J. Li, X. Liao, R. Lu, C. Ling, X. Liu, J. Meng, L. Qu, M. Lin, X. Hong, X. Zhou, S. Liu, Y. Zhao, L. Zhou and L. Mai, *Adv. Mater.*, 2022, **34**, 2200270.
42 W. Zhang, M. Niu, J. Yu, S. Li, Y. Wang and K. Zhou, *Adv. Funct. Mater.*, 2023, **33**, 2302014.
43 Q. Wu, J. Liang, M. Xiao, C. Long, L. Li, Z. Zeng, A. Mavrič, X. Zheng, J. Zhu, H.-W. Liang, H. Liu, M. Valant, W. Wang, Z. Lv, J. Li and C. Cui, *Nat. Commun.*, 2023, **14**, 997.
44 Z. Gai, W. Lin, J. D. Burton, K. Fuchigami, P. C. Snijders, T. Z. Ward, E. Y. Tsymbal, J. Shen, S. Jesse, S. V. Kalinin and A. P. Baddorf, *Nat. Commun.*, 2014, **5**, 4528.
45 F. Song and X. Hu, *Nat. Commun.*, 2014, **5**, 4477.
46 Z. Zhang, C. Feng, D. Wang, S. Zhou, R. Wang, S. Hu, H. Li, M. Zuo, Y. Kong, J. Bao and J. Zeng, *Nat. Commun.*, 2022, **13**, 2473.
47 J. Huang, J. Chen, T. Yao, J. He, S. Jiang, Z. Sun, Q. Liu, W. Cheng, F. Hu, Y. Jiang, Z. Pan and S. Wei, *Angew. Chem., Int. Ed.*, 2015, **54**, 8722–8727.
48 J. Liu, Q. Hu, Y. Wang, Z. Yang, X. Fan, L.-M. Liu and L. Guo, *Proc. Natl. Acad. Sci. U. S. A.*, 2020, **117**, 21906–21913.
49 Z. Zhuang, Y. Li, Y. Li, J. Huang, B. Wei, R. Sun, Y. Ren, J. Ding, J. Zhu, Z. Lang, L. V. Moskaleva, C. He, Y. Wang, Z. Wang, D. Wang and Y. Li, *Energy Environ. Sci.*, 2021, **14**, 1016–1028.
50 X. Li, Z. Cheng and X. Wang, *Electrochem. Energy Rev.*, 2021, **4**, 136–145.
51 J. Suntivich, K. J. May, H. A. Gasteiger, J. B. Goodenough and Y. Shao-Horn, *Science*, 2011, **334**, 1383–1385.
52 Y. Zhao, X. Jia, G. Chen, L. Shang, G. I. N. Waterhouse, L.-Z. Wu, C.-H. Tung, D. O'Hare and T. Zhang, *J. Am. Chem. Soc.*, 2016, **138**, 6517–6524.
53 V. Mehar, M. Kim, M. Shipilin, M. Van den Bossche, J. Gustafson, L. R. Merte, U. Hejral, H. Grönbeck, E. Lundgren, A. Asthagiri and J. F. Weaver, *ACS Catal.*, 2018, **8**, 8553–8567.
54 N. Zhang, X. Feng, D. Rao, X. Deng, L. Cai, B. Qiu, R. Long, Y. Xiong, Y. Lu and Y. Chai, *Nat. Commun.*, 2020, **11**, 4066.
55 Q. Han, Y. Luo, G. Liu, Y. Wang, J. Li and Z. Chen, *J. Catal.*, 2022, **413**, 425–433.
56 Y. Luo, Y. Guan, G. Liu, Y. Wang, J. Li and L. Ricardez-Sandoval, *ACS Catal.*, 2024, **14**, 2696–2708.
57 J. Li, G. Liu, B. Ren, E. Croiset, Y. Zhang and L. Ricardez-Sandoval, *J. Catal.*, 2019, **378**, 176–183.
58 K. Chan and J. K. Nørskov, *J. Phys. Chem. Lett.*, 2015, **6**, 2663–2668.
59 S. Xu, Y. Wang and Y. Li, *Phys. Chem. Chem. Phys.*, 2022, **24**, 9930–9935.